Simulation Study Of A Graphene-On-Silicon Microring Resonator Photodetector

Livia Polverari
DEIB
Politecnico di Milano
livia.polverari@mail.polimi.it

Razia Jafari
DEIB
Politecnico di Milano
razia.jafari@mail.polimil.it

Marta Cargnelutti
DEIB
Politecnico di Milano
marta.cargnelutti@mail.polimi.it

Abstract

Graphene photodetectors provide broadband operation and ultrafast carrier response but suffer from weak optical absorption and limited responsivity. This work presents a MATLAB-based simulation study of graphene and germanium photodetectors integrated on a silicon microring resonator platform. Optical transmission characteristics, enhancement factor, responsivity, and noise-equivalent power are analyzed and compared. The results show that resonant cavity enhancement significantly improves detector sensitivity and wavelength selectivity while highlighting the distinct operating characteristics of graphene and germanium photodetectors for compact and high-performance photonic integrated systems.

I. INTRODUCTION

Integrated silicon photonics has become an important technology for high-speed optical communication and photonic integrated systems. Graphene has attracted significant attention for photodetection because of its broadband optical response, ultrafast carrier dynamics, and compatibility with complementary metal-oxide-semiconductor technology. However, the atomic thickness of graphene results in weak interaction with guided optical modes and consequently limits optical absorption and detector responsivity.

Microring resonators offer an effective approach for increasing light confinement and enhancing light–matter interaction within compact dimensions. Under suitable coupling conditions, optical absorption inside graphene can be significantly increased. In this work, MATLAB simulations are employed to investigate the behavior of a graphene-on-silicon microring photodetector and analyze the effect of different device parameters on detector performance.

II. STRUCTURE AND OPERATING PRINCIPLE

The proposed detector consists of a single-layer graphene channel integrated on a silicon microring resonator fabricated on a silicon-on-insulator platform. The graphene layer is encapsulated using hexagonal boron nitride (hBN) to improve carrier mobility and reduce environmental effects. Source and drain metal contacts are connected to the graphene region for electrical signal extraction, while split-gate electrodes independently control the carrier concentration and form the p–n junction necessary for photo-thermoelectric operation. Fig. 1 illustrates the device structure.

The operating principle combines optical resonant enhancement and the photo-thermoelectric effect. Input light propagating through the bus waveguide couples into the microring resonator and circulates inside the cavity at resonance wavelengths.

$$m\lambda = n_{eff}L \tag{1}$$

where m is the resonance order, n_{eff} is the effective refractive index, and L denotes the optical path length. Constructive interference occurs when the cavity satisfies the resonance condition, increasing the optical field intensity within the resonator and enhancing light–matter interaction. Maximum optical absorption occurs under critical coupling conditions:

$$\xi = 1 - \kappa \tag{2}$$

where ξ denotes the round-trip transmission coefficient and κ represents the coupling coefficient.

The round-trip propagation loss inside the resonator can be expressed as

$$\xi = e^{-W\alpha_{SLG}}e^{-2\pi R\alpha_{WG}} \tag{3}$$

where W is the graphene coverage length, α_{SLG} is the graphene attenuation coefficient, R denotes the ring radius, and α_{WG} represents the waveguide attenuation coefficient.

The photoresponse mechanism relies on the photo-thermoelectric effect. Absorbed optical energy heats carriers inside graphene, generating hot electrons and a temperature gradient across the p–n junction region:

$$V_{PTE} = \int S(x)\nabla T_e(x)dx \tag{4}$$

where S denotes the Seebeck coefficient and T_e represents electron temperature. The wavelength-dependent transmitted optical power of the resonator is given by

$$P_{trans} = P_{in} \frac{(1-\kappa) + \xi - 2\sqrt{(1-\kappa)\xi}\cos(\theta)}{1 + (1-\kappa)\xi - 2\sqrt{(1-\kappa)\xi}\cos(\theta)} \tag{5}$$

where P_{in} is the input optical power and θ represents the round-trip phase shift.

The enhancement factor $EF(\lambda)$ characterizes the increase in light–matter interaction inside the microring resonator due to resonant cavity confinement. The higher intra-cavity energy density within the resonator enhances the optical field and increases the interaction between the guided optical mode and graphene.

The detector performance is further characterized by responsivity, which represents the efficiency of converting optical power into electrical output. For graphene photo-thermoelectric photodetectors, voltage responsivity is defined as

$$R_V = \frac{V_{PTE}}{P_{in}} = \frac{\Delta S \cdot \Delta T_e(\lambda)}{P_{\text{in}}} \tag{6}$$

where R_V denotes voltage responsivity, V_{PTE} is the generated photo-thermoelectric voltage, and P_{in} represents the incident optical power.

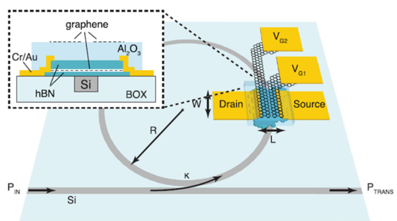

Fig. 1: Schematic structure of the graphene-on-silicon microring resonator photodetector.

III. SIMULATIONS

A. Simulation set-up

In order to demonstrate the benefits and performance improvements of the proposed device, a numerical model is implemented in MATLAB. The simulation is based on the Transfer Matrix Method (TMM) applied to the intra-cavity graphene-on-silicon microring resonator photodetector. The first technology presented here uses material properties, dimensions, and parameters taken from [1], ensuring a physically consistent model. All extracted parameters are reported in Table I. As indicated by the footnotes, the group index n_g and effective index n_{eff} are derived from the experimentally measured FSR. This self-consistent extraction ensures that the simulated resonance wavelength matches the experimental value of $1553.55\,nm$.

TABLE I: Simulation and Experimental Physical Parameters of the Graphene-on-Ring Photodetector

Parameter Details		
Description	**Symbol**	**Value**
Ring Radius	R_{ring}	40 μm
Resonance Wavelength	$\lambda_{\text{res}}^{\text{a,b}}$	1553.55 nm
Free Spectral Range	FSR^{a}	1.45 nm
Group Index	$n_g^{\text{a,b}}$	4.274
Effective Index	$n_{\text{eff}}^{\text{a,b}}$	2.874
Waveguide Propagation Loss	$\alpha_{\text{WG}}^{\text{a}}$	1.4 dB/cm
Power Coupling Coefficient	$(\kappa^2)^{\text{a}}$	0.10
Graphene Absorption Coeff.	$\alpha_{\text{SLG}}^{\text{a}}$	0.07 dB/μm
Optimal Graphene Window	$W_{\text{opt}}^{\text{a}}$	6 μm
Peak Voltage Responsivity	$R_{\text{PTE,peak}}^{\text{a}}$	90 V/W
Seebeck Coeff. Difference	ΔS	200 μV/K
Ambient Temperature	T_0	294 K

[a] From [1] experimental data.
[b] $n_g{=}\lambda_{\text{res}}^2/(\text{FSR}\cdot L)$; $n_{\text{eff}}{=}n_g{+}\lambda\, dn/d\lambda$, correction $\approx{-}1.40$ from [1].

B. Responsivity and Enhancement factor

One key figure of merit of the device is the spectral selectivity of the responsivity. As described in the previous section, in (6), the responsivity of the device is function of the wavelength. If we first consider the case of a simple isolated graphene photodetector, without the ring, although ΔT_e depends in principle on the quantum efficiency and therefore on wavelength, graphene's absorption coefficient α_{SLG} is nearly wavelength-independent, making this dependence negligible in practice. As a result, $R_{V,0}$ is approximately constant across the telecom band, as shown by the blue line in Fig. 2, providing no wavelength selectivity.

On the other hand, when the graphene is integrated inside a silicon microring resonator, the circulating optical field is resonantly enhanced by the intracavity enhancement factor EF(λ), increasing the absorbed power at resonance by EF_{peak} times. The responsivity obtained with the ring is therefore:

$$R_{V,ring}(\lambda) = R_{V,0} \cdot EF(\lambda) \tag{7}$$

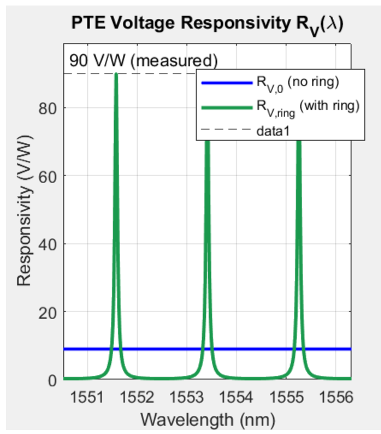

Fig. 2: Voltage responsivity R_V vs. wavelength. Blue: $R_{V,0} \approx 9$ V/W without ring (flat, broadband). Green: $R_{V,\text{ring}}$ peaking at 90 V/W at each resonance ($\text{EF}_{\text{peak}} = 10\times$). Dashed: measured value from [1].

As shown in"Fig. 2", $R_{V,\text{ring}}$ reaches 90 V/W at each resonance (a $10\times$ improvement over $R_{V,0} \approx 9$ V/W) while remaining near zero off-resonance.

Fig. 3 shows the through-port transmission $T(\lambda)$ and the enhancement factor EF(λ) at $W = 6\,\mu$m. The dip at the at λ_{res} reaches -40 dB, confirming a near-perfect critical coupling, while $\text{EF}_{\text{peak}} = 10\times$ drives a proportionally larger PTE voltage.

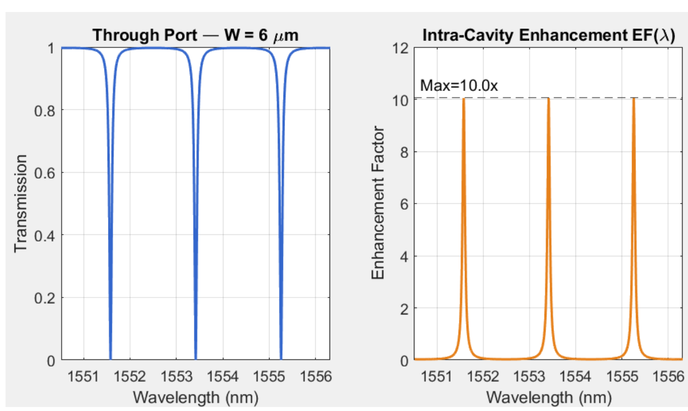

Fig. 3: Left: through-port $T(\lambda)$ at $W = 6\,\mu$m, showing -40 dB extinction at critical coupling. Right: EF(λ) peaking at $10\times$ at the same resonance wavelengths.

C. Noise Equivalent Power of Graphene PTE Detector

For the graphene PTE detector operating at zero bias, the dominant noise mechanism is Johnson thermal noise from the single layer graphene channel resistance $R_G \approx 800\ \Omega$ [1]:

$$v_{noise} = \sqrt{4k_B T R_G} \tag{8}$$

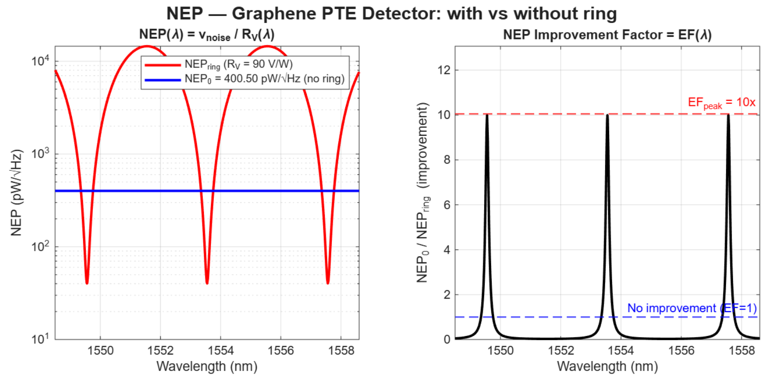

Fig. 4: NEP of the graphene PTE detector. Left: NEP(λ) in pW/$\sqrt{\text{Hz}}$, showing sharp minima at each resonance wavelength with periodicity equal to the FSR of 1.450 nm. Right: NEP improvement factor, confirming $NEP_0/NEP_{ring} = EF(\lambda) = 10\times$ at resonance.

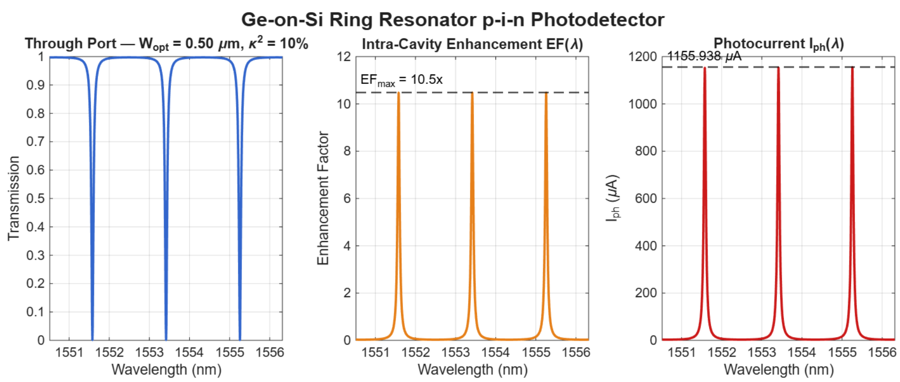

Fig. 5: Spectral response of the Ge-on-Si ring resonator p-i-n photodetector. Left: through port transmission with $W_{opt} = 0.50$ μm. Center: enhancement factor $EF_{max} = 10.5\times$. Right: photocurrent $I_{ph}(\lambda)$ with peak value of 1155.938 μA at $P_{in} = 1$ mW.

Since Johnson noise is independent of optical input power and of the ring enhancement factor, any improvement in responsivity due to the cavity translates directly into an equivalent NEP improvement.

Without the ring, the flat baseline responsivity $R_0 = 9.0$ V/W yields a wavelength-independent NEP floor of $NEP_0 = 400.50$ pW/$\sqrt{\text{Hz}}$. With the ring, the NEP acquires a strong wavelength dependence:

$$NEP_{ring}(\lambda) = \frac{NEP_0}{EF(\lambda)} \tag{9}$$

At $\lambda_{res} = 1553.55$ nm, where $EF_{max} = 10\times$, the NEP drops to ≈ 40 pW/$\sqrt{\text{Hz}}$, a tenfold improvement achieved purely through optical field enhancement, with no modification of the detector material or bias conditions.

D. Noise Equivalent Power of Ge p-i-n Detector

The Ge p-i-n detector produces a photocurrent. The noise is dominated by shot noise from the dark current and Johnson noise from the load resistance $R_{load} = 50\ \Omega$:

$$i_{noise} = \sqrt{2qI_{dark} + \frac{4k_BT}{R_{load}}} \tag{10}$$

with NEP defined as:

$$NEP_{Ge}(\lambda) = \frac{i_{noise}}{R_{Ge}(\lambda)} \tag{11}$$

where $R_{Ge}(\lambda) = EQE_{Ge} \cdot q\lambda/hc$ is the current responsivity computed using the absorption model with $\alpha_{Ge} = 0.8$ dB/μm. Critical coupling is reached at $W_{opt} = 0.50$ μm, significantly shorter than the 6 μm of graphene, reflecting the higher absorption coefficient of germanium on the Silicon-On-Insulator waveguide.

Without the ring, the Ge detector NEP floor is $NEP_0^{Ge} = 163609.588$ fW/$\sqrt{\text{Hz}}$. With the ring, the same $10.5\times$ improvement applies, reducing the NEP to ≈ 15582 fW/$\sqrt{\text{Hz}}$ at resonance.

E. Graphene vs Germanium — Direct Comparison

Table II summarizes the main performance metrics and device characteristics for both detector architectures implemented on the same SOI ring platform.

TABLE II: Comparison of Graphene PTE and Ge p-i-n Ring Detectors

Parameter	**Graphene PTE**	**Ge p-i-n**
Output quantity	Voltage [V/W]	Current [A/W]
Peak responsivity	90 V/W	0.1102 A/W
Noise mechanism	Johnson voltage	Shot + Johnson
NEP_0 (no ring)	400.50 pW/$\sqrt{\text{Hz}}$	163609 fW/$\sqrt{\text{Hz}}$
NEP_{min} (ring)	≈40 pW/$\sqrt{\text{Hz}}$	≈15582 fW/$\sqrt{\text{Hz}}$
NEP improvement	10×	10.5×
Bias required	Zero bias	Reverse ∼1 V
Dark current	Zero	0.12 nA
W_{opt}	6 μm	0.50 μm
Cutoff wavelength	None (broadband)	1880 nm
TIA required	No	Yes

The most significant practical distinction lies in the readout architecture. Converting to consistent units, $NEP_0^{Ge} = 163609$ fW/$\sqrt{\text{Hz}}$ = 163.6 pW/$\sqrt{\text{Hz}}$, comparable to the graphene baseline of 400.50 pW/$\sqrt{\text{Hz}}$. Despite the fundamentally different noise mechanisms, both detectors exhibit similar absolute sensitivity at 1550 nm, with the ring providing the same relative improvement of approximately 10× in both cases. The Ge detector requires a transimpedance amplifier (TIA) to convert photocurrent to voltage, introducing additional power consumption and circuit complexity [1]. The graphene PTE detector directly generates a voltage, which is particularly advantageous for energy-constrained applications such as on-chip optical interconnects in data centers.

As shown in Fig. 3 and Fig. 5, both devices exhibit comparable spectral profiles and identical FSR, differing only in the output quantity: voltage responsivity R[V/W] for graphene versus photocurrent I_{ph} [μA] for Ge.

The wavelength selectivity of the NEP improvement has direct implications for WDM systems. Each detector responds with maximum sensitivity only at its ring resonance wavelength, providing intrinsic channel selectivity without external optical filters. With an FSR of 1.450 nm, multiple ring detectors in cascade, each tuned to a different resonance by slightly varying the ring radius, can implement a complete WDM demultiplexer on a single SOI chip, compatible with C-band channel spacing standards.

IV. Conclusions

In this work, we presented a Transfer Matrix Method simulation of a microring resonator-enhanced photodetector on a silicon-on-insulator platform, based on the device architecture reported in [1]. Two detection materials were systematically investigated on the same ring geometry ($R = 40$ μm, $\kappa^2 = 10\%$, FSR = 1.450 nm): single-layer graphene exploiting the photo-thermoelectric effect, and germanium operating as a conventional p-i-n photodiode.

For the graphene PTE detector, critical coupling at $W_{opt} = 6$ μm yields $EF_{max} = 10\times$ at $\lambda_{res} = 1553.55$ nm, a peak responsivity of 90 V/W, and a tenfold NEP improvement. For the Ge p-i-n detector, $W_{opt} = 0.50$ μm and $EF_{max} = 10.5\times$ provide a comparable NEP improvement, confirming that cavity enhancement is material-independent.

The two architectures present complementary strengths: graphene offers zero-bias operation, zero dark current, direct voltage output without TIA, and broadband spectral coverage; germanium offers higher fabrication maturity and CMOS compatibility. In both cases, the ring resonator provides intrinsic wavelength selectivity enabling WDM channel demultiplexing on chip without external optical filters, representing a compelling architecture for next-generation data center optical interconnects operating in the C-band.

References

[1] S. Schuler, J. E. Muench, A. Ruocco, O. Balci, D. van Thourhout, V. Sorianello, M. Romagnoli, K. Watanabe, T. Taniguchi, I. Goykhman, A. C. Ferrari, and T. Mueller, "High-responsivity graphene photodetectors integrated on silicon microring resonators," *Nat. Commun.*, vol. 12, June 2021.

[2] L. Alloatti and R. J. Ram, "Resonance-enhanced waveguide-coupled silicon-germanium detector," *Appl. Phys. Lett.*, vol. 108, no. 7, Feb. 2016.

[3] A. Chatterjee, S. Yadav, S. K. Sikdar, and S. K. Selvaraja, "Compact ring resonator enhanced silicon metal-semiconductor-metal photodetector in SiN-on-SOI platform," *Opt. Express*, vol. 28, no. 22, Oct. 2020.

[4] J. F. Liu, D. Ahn, C. Y. Hong, D. Pan, S. Jongthammanurak, M. Beals, L. C. Kimerling, J. Michel, A. T. Pomerene, D. Carothers, C. Hill, M. Jaso, K. Y. Tu, Y. K. Chen, S. Patel, M. Rasras, D. M. Gill, and A. E. White, "Waveguide-integrated Ge p-i-n photodetectors," *IEEE Journal of Selected Topics in Quantum Electronics*, vol. 13, no. 1, Jan.–Feb. 2007.

[5] J. E. Muench, M. Ruocco, M. A. Giambra, O. Balci, D. van Thourhout, V. Sorianello, M. Romagnoli, I. Goykhman, A. C. Ferrari, and T. Mueller, "Waveguide-integrated plasmonic enhanced graphene photodetectors," *Nano Letters*, vol. 19, no. 11, pp. 7632–7644, 2019.